**Smart Structures and Systems**, *Vol. 23, No. 1 (2019) 91-106*
DOI: https://doi.org/10.12989/sss.2019.23.1.091


# Real-time hybrid simulation of smart base-isolated raised floor systems for high-tech industry

Pei-Ching Chen[*1], Shiau-Ching Hsu[2a], You-Jin Zhong[2b] and Shiang-Jung Wang[1c]

[1]*Department of Civil and Construction Engineering, National Taiwan University of Science and Technology, No.43, Sec.4, Keelung Rd., Taipei 10607, Taiwan*
[2]*Department of Civil Engineering, National Taiwan University, No.1, Sec. 4, Roosevelt Rd., Taipei 10617, Taiwan*

*(Received September 19, 2018, Revised December 8, 2018, Accepted December 17, 2018)*

**Abstract.** Adopting sloped rolling-type isolation devices underneath a raised floor system has been proved as one of the most effective approaches to mitigate seismic responses of the protected equipment installed above. However, pounding against surrounding walls or other obstructions may occur if such a base-isolated raised floor system is subjected to long-period excitation, leading to adverse effects or even more severe damage. In this study, real-time hybrid simulation (RTHS) is adopted to assess the control performance of a smart base-isolated raised floor system as it is an efficient and cost-effective experimental method. It is composed of multiple sloped rolling-type isolation devices, a rigid steel platen, four magnetorheological (MR) dampers, and protected high-tech equipment. One of the MR dampers is physically tested in the laboratory while the remainders are numerically simulated. In order to consider the effect of input excitation characteristics on the isolation performance, the smart base-isolated raised floor system is assumed to be located at the roof of a building and the ground level. Four control algorithms are designed for the MR dampers including passive-on, switching, modified switching, and fuzzy logic control. Six artificial spectrum-compatible input excitations and three slope angles of the isolation devices are considered in the RTHS. Experimental results demonstrate that the incorporation of semi-active control into a base-isolated raised floor system is effective and feasible in practice for high-tech industry.

**Keywords:** raised floor system; sloped rolling-type isolation device; magnetorheological damper; semi-active control; real-time hybrid simulation

## 1. Introduction

Raised floor systems have been widely assembled in modern buildings, particularly for, data centers, emergency control centers, commercial banks, telecommunication central offices, and high-tech fabrication laboratories. It is known that raised floor systems are elevated above building slabs; therefore, concealed space can be created for routing electrical cables and allocating facilities, air conditioning systems, and measurement sensors. Since raised floors are installed at a certain height from the slab, additional structural support and lighting system are required. Damages of industrial facilities were observed during the 1999 Chi-Chi earthquake in Taiwan due to the failure of raised floor systems even though the buildings still remained intact. During the past decades, high-tech companies have learned from the earthquakes that enormous pecuniary loss due to the malfunction of facilities could be several times the cost of the facilities after an earthquake. Therefore, it has become a significant issue to increase the seismic resistance of raised floor systems in high-tech industry.

Seismic isolation technology has been regarded as an effective approach to mitigate seismic risks and potential damages of high-tech equipment and facilities (Liao *et al*. 2013). In particular, sloped rolling-type isolation devices have been demonstrated to effectually reduce the acceleration transmitted to the raised floor system (Wang *et al*. 2014). Typically, the sloped rolling-type isolation device is composed of three bearing plates, two pairs of rollers, and four side plates as illustrated in Fig. 1(a). From the top to the bottom, the three bearing plates are referred to as upper, intermediate, and lower plates, respectively. One of the surfaces of upper and lower plates that contacts the rollers can be either dual V-shape or flat. However, both surfaces of the intermediate plate are dual V-shape. In each horizontal direction, a pair of rollers can be rolling back and forth between two bearing plates simultaneously, providing in-plane seismic isolation capability with synchronized movement. Originally, damping of the sloped rolling-type isolation devices is contributed from the rolling friction; however, the inherent rolling friction is insignificant and can be neglected generally. Pounding against surrounding walls or other obstructions may occur if the sloped rolling-type isolation device is exposed to long-period excitation

∗Corresponding author, Assistant Professor
E-mail: peichingchen@mail.ntust.edu.tw
[a] Graduate Student
E-mail: r06521202@ntu.edu.tw
[b] Graduate Student
E-mail: r06521207@ntu.edu.tw
[c] Associate Professor
E-mail: sjwang@mail.ntust.edu.tw


http://www.techno-press.com/journals/sss&subpage=7 ISSN: 1738-1584 (Print), 1738-1991 (Online)

such as the floor acceleration response at high-rise buildings subjected to earthquakes. In order to increase the damping, additional sliding friction force can be generated between the side plate and bearing plate. By embedding adjustable linear springs in the side plates, the normal force between the side plate and bearing plate can be tuned such that the designed sliding friction can be realized (Wang *et al*. 2014). It is noted that the normal force between the side plate and bearing plate is in the horizontal direction; therefore, it is not affected by the mass on the isolation device. Consequently, significant displacement responses under severe earthquakes can be suppressed successfully by increasing the sliding friction. However, the acceleration transmitted to the raised floor system increases when the sliding friction force increases. There exists a tradeoff between the transmitted acceleration and the displacement response of the sloped rolling-type isolation device. As a result, the isolation devices incorporated into active or semi-active control, which are generally referred as smart isolation system (Ramallo *et al*. 2002, Bahar *et al*. 2018) may provide a solution for mitigating the seismic responses of raised floor systems subjected to long-period excitation.

Real-time hybrid simulation (RTHS) has been recognized as an efficient and cost-effective testing method for investigating seismic responses of structural systems (Shao *et al*. 2014, Friedman *et al.* 2015, Zhang *et al.* 2017). Part of a structural system which contains components that are difficult to analytically simulate is experimentally tested in the laboratory whereas the rest parts are numerically simulated using finite element method or other analytical approaches. The interface between the experimental and numerical parts is formed by using servo-hydraulic actuators and appropriate fixtures. Typically, a step-by-step integration algorithm is employed to attain the displacement response at the interface which is treated as the desired response to be imposed on the experimental substructure. The force response is then measured from the experimental substructure and sent back to the integration algorithm to calculate the displacement response at the interface for the next time step until the RTHS is completed. It is noted that the responses at the interface must be imposed on the experimental substructure by servo-hydraulic actuators in real time. Any time lag and delay introduces negative damping into a RTHS, leading to inaccurate test results or simulation divergence (Horiuchi *et al*. 1999). In order to resolve this issue, various delay compensation methods have been developed including polynomial extrapolation (Darby *et al*. 2002), derivative feedforward compensation (Jung *et al*. 2007), adaptive compensation (Chae *et al*. 2013), and optimal discrete-time compensation (Hayati and Song 2017). These aforementioned methods have been demonstrated to achieve successful RTHS.

In this study, RTHS is adopted as an experimental tool to evaluate the seismic performance of a smart based-isolated raised floor system located at two elevation levels of a building. The sloped rolling-type isolation devices are applied to isolate the floor excitation input to the raised floor system. Meanwhile, magnetorheological (MR) dampers are adopted to provide the semi-active controllability for the isolation devices. Without loss of generality, nine sloped rolling-type isolation devices distributed evenly underneath a raised floor with 300-mm isolation clearance are assumed in the study. For RTHS, the sloped rolling-type isolation devices, raised-floor system, and equipment to be protected are numerically simulated whereas one of the MR dampers is physically tested. Four control algorithms are designed and applied to the smart base-isolated raised floor system to investigate the seismic performance on acceleration and displacement responses transmitted to the raised floor. Meanwhile, three slope angles of the isolation device are adopted for RTHS in order to assess the control performance affected by slope angles. Furthermore, six artificial acceleration time histories compatible to the AC156 required response spectrum (RRS) (AC156 2010) are generated to evaluate the influence of various excitation characteristics on the control performance. Hence, a total number of 72 RTHSs are completed. Finally, the control performances of all the cases are compared mutually and discussed thoroughly.

## 2. Numerical model

A raised floor system with sloped rolling-type isolation devices and MR dampers is adopted for the case of study. Nine sloped rolling-type isolation devices distributed evenly underneath the raised floor with 300-mm isolation clearance in the horizontal direction are assumed in the study.

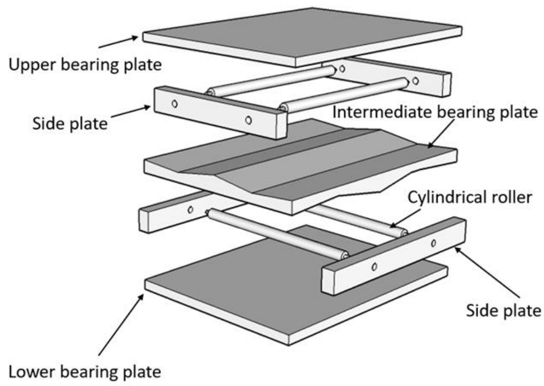


(a) Schematic view

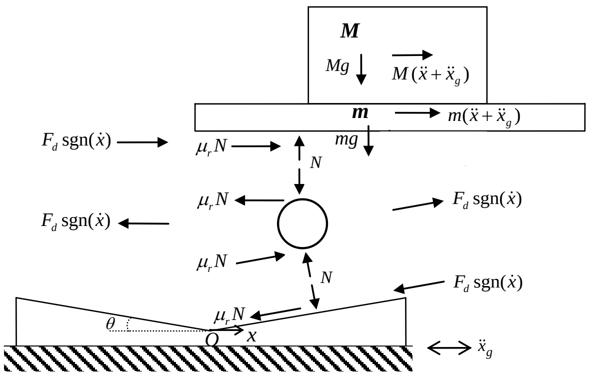


(b) Free body and kinetic diagrams

Fig. 1 Illustration of the sloped rolling-type isolation device

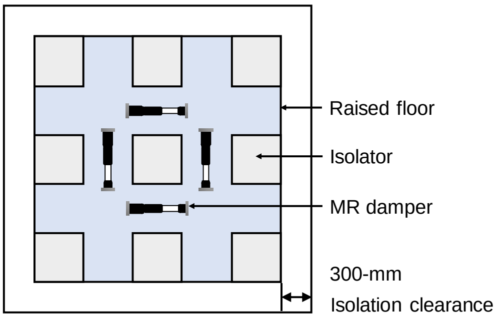


(a) Top view

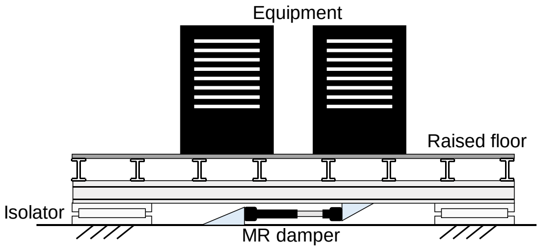


(b) Front view

Fig. 2 Illustration of the smart base isolation raised floor system

The isolation devices are placed at the bottom of the raised floor to isolate the excitation from the floor while two pairs of MR dampers are installed in two orthogonal directions to semi-actively control the isolated system. The schematics of the smart base-isolated raised floor system is depicted in Fig. 2. The mass of the equipment on the raised floor is set 1500 N-s$^2$/m. Namely, each sloped rolling-type isolation device takes a mass of 166.67 N-s$^2$/m. For safety concerns, numerical simulation of the proposed smart base-isolated raised floor system needs to be performed before conducting RTHS in the laboratory. Therefore, the numerical models of the isolation device and MR damper need to be built first which will be introduced in this session.

### *2.1 Sloped rolling-type isolation device*

The mathematical model of the sloped rolling-type isolation device has been developed and verified (Wang *et al*. 2014). As depicted in Fig. 1(a), each single roller of the device is allocated between a flat surface and a V-shaped surface with a slope angle of $\theta$ in the principle horizontal direction. It is noted that the rolling mechanism on a bevel results in vertical acceleration transmitted to the protected equipment; however, the contribution has been considered negligible (Wang *et al*. 2017). By neglecting the effect of the vertical ground acceleration, the simplified equation of motion of the sloped rolling-type isolation device in the horizontal direction when the rollers are moving on the bevel can be represented as

$$\ddot{x}+\ddot{x}_g=-\frac{1}{2}g\sin\theta\,\mathrm{sgn}(x)-\frac{[\mu_r N+F_d]}{M+m}\mathrm{sgn}(\dot{x}) \qquad (1)$$

where $x$ is the relative displacement between the isolation device and the floor; $\ddot{x}_g$ is the acceleration that is input to the isolation device; $g$ represents the gravity; $M$ and $m$ are the distributed mass of the protected equipment, and the overall mass of the device above the rollers, respectively; $\mu_r$ is the ratio of the rolling resistant coefficient between the roller and the slope surface; $N$ is the normal force acting between the rollers and the bearing plates; and $F_d$ is the inherent damping force of the device due to sliding friction between the side plate and the bearing plate. The parameters aforementioned are illustrated by simply using free body and kinetic diagrams of a single roller sandwiched between a flat surface and a V-shaped surface, as shown in Fig. 1(b). On the other hand, when the rollers are moving within the fixed curvature range, the simplified equation of motion of the sloped rolling-type isolation device in the horizontal direction can be expressed as

$$\ddot{x}+\ddot{x}_g=-\frac{g}{4R}x-\frac{[\mu_r N+F_d]}{M+m}\mathrm{sgn}(\dot{x}) \qquad (2)$$

where $R$ is the fixed curvature radius between two inclines of the V-shaped surface. The ratio of the rolling resistant coefficient ($\mu_r$) was 0.002. The inherent damping force ($F_d$) of the device was 10 N. The equipment mass distributed to each isolation device ($M$) was 166.67 N-s$^2$/m. The overall mass of the device above the rollers ($m$) was 48 N-s$^2$/m. The fixed curvature radius was 0.1 m.

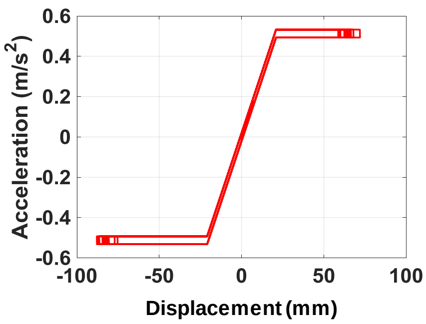


(a) Without inherent damping

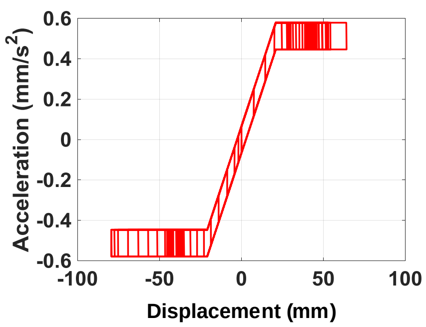


(b) With inherent damping

Fig. 3 Displacement-acceleration relationship of the numerical model of the isolation device

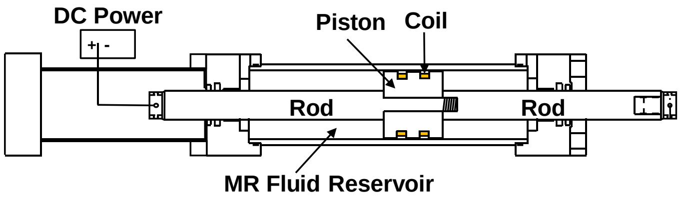


Fig. 4 The structure of the MR damper used in this study

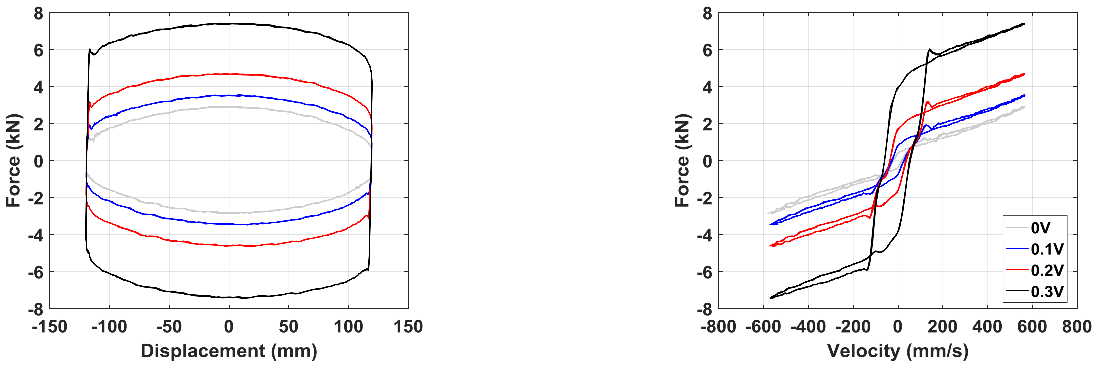


(a) Displacement-to-force relationship (b) Velocity-to-force relationship

Fig. 5 Experimental responses of the MR damper

For example, the transmitted absolute acceleration of the isolation device without inherent damping force is about 0.55 m/s$^2$ when the slope angle is 6 degrees. Fig. 3 depicts the displacement-acceleration relationship of the isolation device model with and without inherent damping force when the slope angle is 6 degrees. The excitation acceleration was a sinusoidal wave with an amplitude of 1.0 m/s$^2$ and a frequency of 1 Hz. From Fig. 3, it can be found that larger damping force results in smaller displacement but larger acceleration.

### *2.2 Magnetorheological damper*

The MR damper specimen employed in this study was designed and fabricated by the National Center for Research on Earthquake Engineering (NCREE) in Taiwan in 2017. It is double-ended with two coils in the piston as shown in Fig. 4. The maximum nominal force and stroke capacities of the MR damper are ±7 kN and ±125 mm, respectively. The responses of the MR damper subjected to 0.75-Hz, 120-mm sinusoidal displacement with a variety of input voltages are shown in Fig. 5. From the tests, it was realized that the maximum control voltage was 0.3 V.

In order to model the MR damper, the Bouc-Wen hysteresis operator-based dynamic model was used. The MR damper force can be described as

$$F_{MR}(t) = C(v)\dot{x}(t) + z(t) \tag{3}$$

where $F_{MR}$, and $v$, are the force, and control voltage of the MR damper, respectively; the parameter $C$ is the damping coefficient which is a function of the control voltage $v$; and $z$ is the hysteretic parameter of the Bouc-Wen Model and can be expressed as

$$z(t) = \alpha\dot{x}(t) + \beta|\dot{x}(t)||z(t)|^{n-1}z(t) + \gamma\dot{x}(t)|z(t)|^{n} \tag{4}$$

where the parameters $\alpha$, $\beta$, $\gamma$, and $n$ shape the hysteresis loop. In order to conduct numerical simulation, Eqs. (3) and (4) were further converted into discrete time as

$$F_{MR}[k] = C(v[k])\dot{x}[k] + z[k] \tag{5}$$

$$z[k] = z[k-1] + \left[\alpha\dot{x}[k] + \beta|\dot{x}[k]||z[k-1]|^{n-1}z[k-1] + \gamma\dot{x}[k]|z[k-1]|^{n}\right]\cdot\Delta t \tag{6}$$

where $k$ represents the k$^{th}$ step, and $\Delta t$ is the sampling period of the data. In order to get the numerical model of the MR damper, various input excitations were adopted for the performance tests. First, sine waves with four frequencies at three amplitude levels were used. Seven constant voltages were considered for the MR damper under each input excitation. Then, the "fimincon" function provided by MATLAB was used to obtain the most appropriate parameters for the Bouc-Wen model to simulate the MR damper. Finally, incremental sinusoidal excitations were adopted to verify the accuracy of the identified numerical model. Fig. 6 depicts the displacement-force relationship, velocity-force relationship, and a part of force time history of the responses of MR damper experimentally and numerically with a control voltage of 0.3 V under a sinusoidal displacement excitation with a frequency of 0.5 Hz and incremental amplitudes. It can be found that the experimental and simulation results do not fit with each other perfectly, yet acceptably.

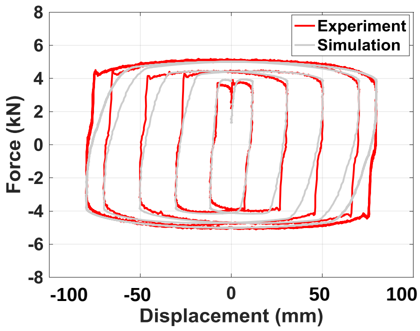


(a) Displacement-to-force relationship

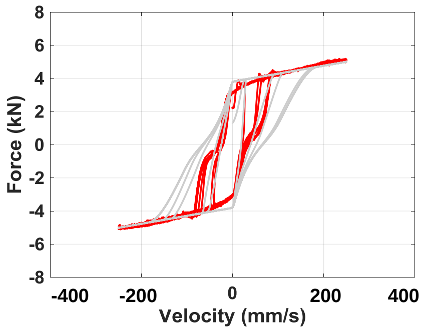


(b) Velocity-to-force relationship

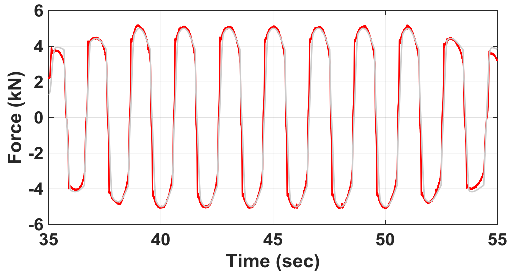


(c) Force time history

Fig. 6 Comparison of experimental and numerical responses of the MR damper

## 3. MR damper controller design

Controller design is crucial for the effectiveness of control performance of a MR damper. Various control algorithms for MR dampers have been proposed and implemented to suppress seismic responses of structural/nonstructural systems both in numerical and experimental studies such as linear-quadratic regular (Dyke *et al*. 1996), modal control (Cho *et al*. 2005), sliding mode control (Zheng and Li 2009), and adaptive control (Javanbakht and Amini 2016). In this study, four control algorithms were designed and applied to the base-isolated raised floor system to control its seismic response including passive-on control (a maximum control voltage of 0.3 V was retained), switching control (SC), modified switching control (MSC), and fuzzy logic control (FLC).

### *3.1 Switching control*

From the equation of motion of the sloped rolling type isolation device as indicated in Eq. (1) and (2), it is known that larger damping force results in larger transmitted acceleration. As a result, switching control (SC) provides a simple approach to control the force response of MR dampers. When the isolation device is moving away from the original position, the control voltage is set 0 V. Accordingly, the transmitted acceleration is not enlarged at this stage. On the other hand, when the isolation device changes its direction, the control voltage is switched to a maximum voltage (0.3 V). Hence, the damper force can dissipate the energy effectively without increasing the transmitted acceleration. The control algorithm can be described as

$$\begin{aligned} v &= 0\ \mathrm{V} \quad && \textit{when}\ \operatorname{sgn}(x\cdot\dot{x})\geq 0 \\ v &= 0.3\ \mathrm{V} \quad && \textit{when}\ \operatorname{sgn}(x\cdot\dot{x})<0 \end{aligned} \tag{7}$$

Fig. 7(a) illustrates the switching of control voltage.

### *3.2 Modified switching control*

The control criterion of the modified switching control (MSC) is very much similar to that of the SC; however, the control voltage is set 0 V merely before the relative displacement of the isolation device exceeds 100 mm. Then, the control voltage is linearly increased with a ramping rate of 0.006 V/mm until it reaches the maximum control voltage 0.3 V. In other words, the control voltage reaches to 0.3 V when the relative displacement is equal or lager than 150 mm. The MSC algorithm can be expressed as

$$\begin{aligned} & v = 0\ \mathrm{V} \\ & v = 0.006\cdot\left(|x|-100\right)\ \mathrm{V} \\ & v = 0.3\ \mathrm{V} \\ & \textit{when}\left(\operatorname{sgn}(x\cdot\dot{x})\geq 0\right)\cap\left(|x|\leq 100\ mm\right) \\ & \textit{when}\left(\operatorname{sgn}(x\cdot\dot{x})\geq 0\right)\cap\left(100\ mm\leq|x|\leq 150\ mm\right) \\ & \textit{when}\left(\operatorname{sgn}(x\cdot\dot{x})<0\right)\cup\left(\left(\operatorname{sgn}(x\cdot\dot{x})\geq 0\right)\cap\left(|x|\geq 150\ mm\right)\right) \end{aligned} \tag{8}$$

The modified switching control is depicted in Fig. 7(b). It can be found that the MSC is identical to the SC if the displacement is always smaller than 100 mm. Furthermore, the MSC is equal to passive-on control when the displacement is larger than 150 mm. As a result, it can be

Table 1 The fuzzy rule base

| Control voltage | | Displacement | | | | | |
|---|---|---|---|---|---|---|---|
| | | NL | NS | NZR | PZR | PS | PL |
| Velocity | NL | NL | NM | ZR | PM | PL | PL |
| | NS | NM | ZR | ZR | PS | PM | PL |
| | NZR | ZR | ZR | ZR | PS | PM | PL |
| | PZR | NL | NM | NS | ZR | ZR | ZR |
| | PS | NL | NM | NS | ZR | ZR | PM |
| | PL | NL | NL | NM | ZR | PM | PL |

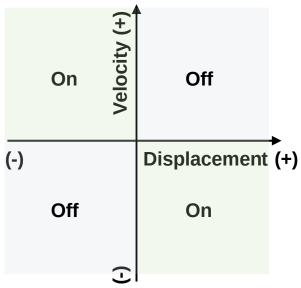


(a) Switching control

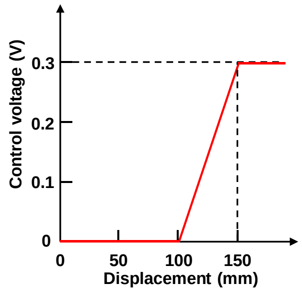


(b) Modified switching control when $\mathrm{sgn}(x \cdot \dot{x}) \geq 0$

Fig. 7 Illustration of the switching control

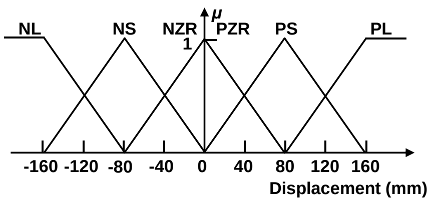


(a) Input displacement

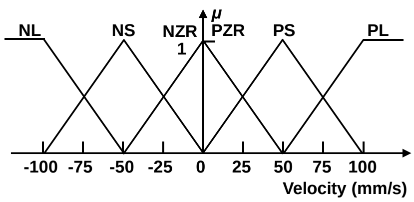


(b) Input velocity

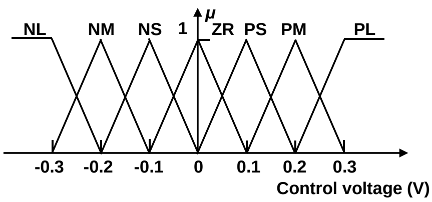


(c) Output control voltage

Fig. 8 Membership functions for fuzzy logic control

expected that the control performance of the MSC should be in between that of the SC and passive-on control.

### *3.3 Fuzzy logic control*

Fuzzy logic control (FLC) has been recognized as a simple method in designing controllers which consider system nonlinearity since it was first implemented by Mamdani in 1974. In this study, the membership functions for the FLC are formed by engineering sense and experience without applying any optimization methods because prompt design and implementation are essential for real practice in high-tech industry. The relative displacement and the relative velocity are adopted as the input states, and the corresponding input space can be described as a membership value between 0 and 1. In this study, the control targets are aimed at suppressing the displacement of the sloped rolling-type isolation device as well as decreasing its transmitted acceleration. As a result, the triangular membership functions can be defined through trial and error as shown in Fig. 8. It is noted that the negative control voltage is replaced by positive control voltage in the numerical simulation. The fuzzy rule base is shown in Table 1 where NL, NM, NS, NZR, PZR, PS, PM,

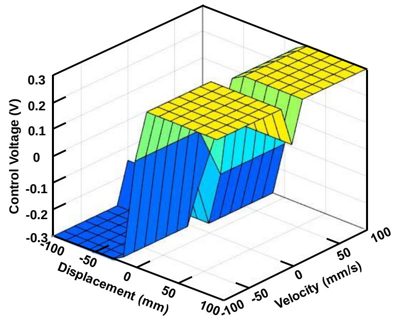


Fig. 9 The rule surface of the fuzzy logic controller

and PL represent negative large, negative medium, negative small, negative zero, positive zero, positive small, positive medium, and positive large, respectively. Mamdani's method is used for fuzzy inference. For defuzzification, the center of area method is adopted. The surface of the fuzzy rule base is depicted in Fig. 9.

## 4. Analytical studies

MATLAB/Simulink was used to perform the analytical simulation of the smart base-isolated raised floor system before applying RTHS in the laboratory for safety concerns. Four major components were considered in the simulation including sloped rolling-type isolation devices, rigid equipment placed on the raised floor, a MR damper and its controller, and dynamics of the servo-hydraulic system. It is noted that since a rigid mass was used to represent the equipment; therefore, the acceleration on the raised floor was assumed identical to that on the top of the isolators. The ode4 solver using the Runge-Kutta formula was adopted for the simulation. All the simulations were computed using a sampling rate of 200 Hz. As Fig. 2 indicates, the raised floor system is supported by nine sloped rolling-type isolation devices. The mass of the equipment placed on the raised floor was 1500 N-s$^2$/m, which indicates that each isolation device takes a mass of 166.67 N-s$^2$/m. The stroke of the MR damper was ±125 mm, which was not large enough to describe the assumed 300-mm isolation clearance. In addition, the MR damper force was ±7 kN, which was not large enough to control the raised floor system with heavy equipment. Therefore, the maximum stroke and force of the MR damper in the numerical model were enlarged 3 times.

The equations of motion of the smart base-isolated raised floor system when the rollers are moving within the sloped surface can be expressed as

$$\ddot{x}+\ddot{x}_g=-\frac{1}{2}g\sin\theta\,\mathrm{sgn}(x)-\frac{[\mu_r N+F_d]}{M+m}\mathrm{sgn}(\dot{x})+\frac{F_{MR}}{M+m} \quad (9)$$

Similarly, when the rollers are moving within the fixed curvature range, the equation of motion can be expressed as

$$\ddot{x}+\ddot{x}_g=-\frac{g}{4R}x-\frac{[\mu_r N+F_d]}{M+m}\mathrm{sgn}(\dot{x})+\frac{F_{MR}}{M+m} \quad (10)$$

In addition, it was observed that both slipping and sticking occur at the sloped rolling-type isolation device during an earthquake excitation (Wang *et al.* 2014). The equations of motion given in Eqs. (9) and (10) are applicable only when the relative velocity of the isolation device is not zero. In other words, Eqs. (9) and (10) are valid only when the inertia force, MR damper force, and external disturbance such as earthquake ground motions are large enough to conquer the friction force. Therefore, the isolation device is able to move instead of sticking. However, the isolation device remains in rest when these forces are too slight to prevail against the friction force. As a result, the motion of the isolation device can be approximated fairly by following additional two conditions whenever the relative velocity is changing the direction between the current step and the previous step as

$$\ddot{x}=\dot{x}=0$$
$$when\ \left|\ddot{x}_g+\frac{1}{2}g\sin\theta\,\mathrm{sgn}(x)-\frac{F_{MR}}{M+m}\right|\le\left|\frac{\mu_r N+F_d}{M+m}\right| \quad (11)$$

while the rollers are moving on the bevel; or

$$\ddot{x}=\dot{x}=0$$
$$when\ \left|\ddot{x}_g+\frac{g}{4R}x-\frac{F_{MR}}{M+m}\right|\le\left|\frac{\mu_r N+F_d}{M+m}\right| \quad (12)$$

while the rollers are moving within the fixed curvature range.

In order to understand the effect of the slope angles of the isolation device on the seismic response, three different slope angles (3, 6, and 9 degrees) were considered in the simulation. In addition, six artificial input floor excitations compatible to the AC156 required response spectrum, rather than floor responses obtained by straightforwardly using an arbitrary building model, were adopted to have more generalized and representative analytical results and discussions. With the information of the height in structure of point of attachment of component with respect to the base, as well as the average roof height of structure with respect to the base, the floor responses considering the

Table 2 Maximum relative displacement and absolute acceleration of the numerical simulation results ($\theta$=6$^o$)

| Input excitation | Control algorithm | Maximum relative displacement (mm) | Maximum absolute acceleration (m/s$^2$) |
|---|---|---|---|
| TAP034_1F | Passive-on | 88.62 | 1.470 |
| | SC | 126.67 | 0.934 |
| | MSC | 125.74 | 0.949 |
| | FLC | 126.38 | 1.276 |
| TAP034_RF | Passive-on | 234.59 | 1.540 |
| | SC | pounding | pounding |
| | MSC | 263.60 | 1.557 |
| | FLC | 269.99 | 1.545 |
| TCU061_1F | Passive-on | 109.00 | 1.510 |
| | SC | 145.96 | 0.955 |
| | MSC | 137.38 | 1.117 |
| | FLC | 114.78 | 1.248 |
| TCU061_RF | Passive-on | 210.85 | 1.623 |
| | SC | pounding | pounding |
| | MSC | 272.17 | 1.519 |
| | FLC | 258.40 | 1.482 |
| KAU062_1F | Passive-on | 117.43 | 1.490 |
| | SC | 147.47 | 0.946 |
| | MSC | 142.38 | 1.205 |
| | FLC | 131.58 | 1.301 |
| KAU062_RF | Passive-on | 243.58 | 1.585 |
| | SC | 294.34 | 1.031 |
| | MSC | 246.43 | 1.581 |
| | FLC | 248.37 | 1.562 |

dynamic amplification of the building structure can be rationally obtained. Based on the assumption that the isolated raised floor system and the equipment above are much lighter than the building structure, their dynamic interaction can be negligible reasonably. With the phase spectrum modeled by integrating the simulated group delay times, and through the iteration process of modifying Fourier amplitude, an artificial acceleration time history whose acceleration response spectrum matches the target response spectrum can be generated (Chai *et al.* 2002). The acceleration time histories were generated based on three historical ground acceleration records in the Chi-Chi earthquake in 1999, namely TAP034, TCU061, and KAU062. Considering that the transmitted acceleration could be amplified by the dynamics of buildings, two artificial acceleration time histories were generated from each historical ground acceleration records to respectively represent the floor acceleration responses at the ground level (1F) and the roof of a building (RF).

Finally, six artificial input excitations were adopted, namely TAP034_1F, TAP034_RF, TCU061_1F, TCU061_0RF, KAU062_1F, and KAU062_RF. Summarily, there were four control algorithms, three slope angles, and six input excitations, leading to a total number of 72 cases in the numerical simulation.

Due to the page limitation, only the cases with a slope angle of 6 degrees are summarized in this section. The maximum relative displacement and absolute acceleration of the isolation device ($\theta$=6$^o$) subjected to the aforementioned artificial ground motions are shown in Table 2. The relative displacements of the SC were significant and even exceeded the isolation clearance in some cases, which was supposed to have pounding in real practice. Passive-on control (maximum control voltage was retained) regularly resulted in reasonable relative displacements; however, the absolute accelerations increased due to the additional damping, which may not be acceptable for isolation. Compared with the passive-on control performance, the transmitted acceleration of the raised floor system can be reduced for the other three controllers. The performances of the MSC and FLC were similar. The relative displacements remained within the isolation clearance and the absolute accelerations were mostly smaller than those of the passive-on control method.

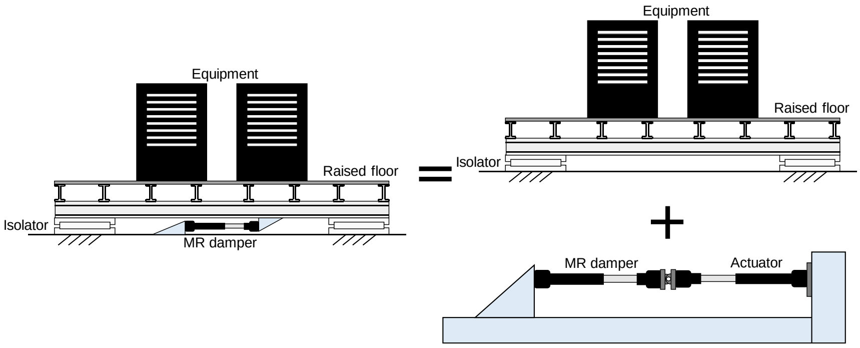


Fig. 10 Schematic of the numerical and experimental substructures of the smart base-isolated raised floor system

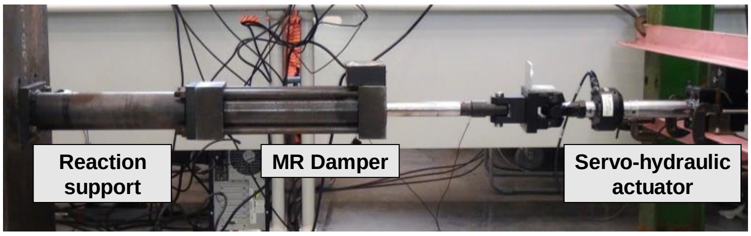


Fig. 11 Experimental setup of the RTHS

However, the displacement was not suppressed in most cases compared with the passive-on control approach. It is observed that the MSC and FLC result in balanced control performance between the absolute acceleration and relative displacement for all the simulation cases. Consequently, the numerical simulation results provide a prior knowledge on the control performance of each control algorithms. Then, the overall control performance can be assessed thoroughly by conducting RTHS.

## 5. Real-time hybrid simulation

The schematic of the smart base-isolated raised floor system is shown in Fig. 10 in which the experimental substructure is one of the MR dampers. The numerical substructure consists of the sloped rolling-type isolation devices, the raised floor, and the equipment installed above. The experimental test setup is shown in Fig. 11. The MR damper is pin-connected to a 15-kN dynamic servo-hydraulic actuator at one end, and the other end is connected to a reaction support. The displacement computed from the numerical model was 1/3 scaled down as the desired displacement of the MR damper. The corresponding measured force of the MR damper was 3-time scaled up and sent back to the numerical model to compute the response for the next time step. Similar to the numerical studies, a total number of 72 cases were evaluated by the RTHS results.

### *5.1 Hardware and software layout*

The experimental layout for RTHS in this study is composed a dSPACE MicroLabBox and an MTS-FT100 digital controller. The MicroLabBox is an integrated system which is equipped with more than 100 input/output channels of different types. In addition, the input/output latencies of the MicroLabBox are extremely low and can be neglected, providing excellent real-time execution performance. Furthermore, the MicroLabBox is well-supported by Real-Time Interface (RTI) for MATLAB/Simulink. RTI provides blocks in the Simulink model with the input/output capabilities. GNU C compiler is then used to compile the real-time model and generate executable object code for the MicroLabBox processors. Meanwhile, an experiment software ControlDesk is used to access the real-time application during the RTHS with a user-friendly interface. Control gains can be tuned in real time thorough the ControlDesk software. On the other hand, the MTS-FT100 digital controller can receive external signals from the MicroLabBox to drive the actuator in displacement control mode. It also sends the measured displacement and force of the MR damper to the MicroLabBox for computing the response for the next step. Fig. 12 illustrates the hardware and software layout for the RTHS. In this study, the base-isolated raised floor system except the MR dampers is numerically simulated by a Simulink model with real-time input/output blocks. It is noted that the MR damper response force depends on the input current level. However, the MR damper control command computed from the MicroLabBox is a voltage signal with negligible small current. Therefore, an instrument that can convert the computed control voltage to a control current is required. In the RTHS, a voltage control current source (VCCS), manufactured by Lord Cooperation, Cary, North California, was adopted. The VCCS was used to generate a control current to the MR damper that was linearly related to the computed control voltage from the

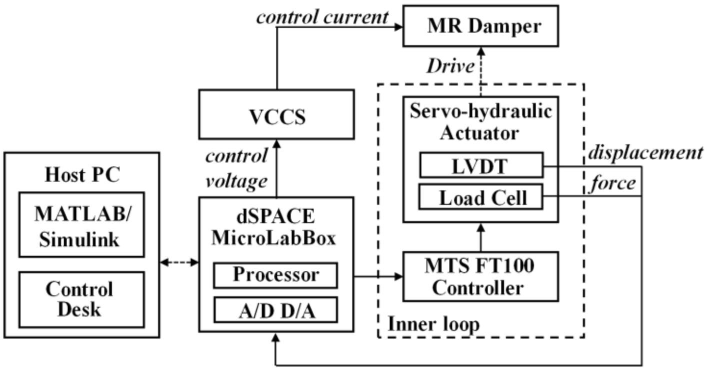


Fig. 12 Hardware and software layout for RTHS

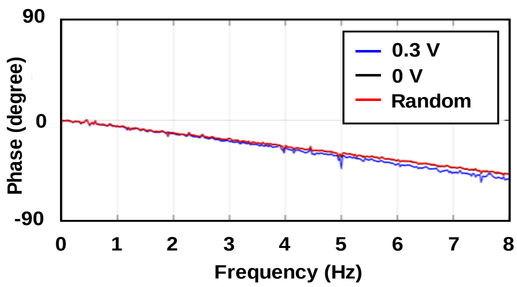


Fig. 13 Phase plot between desired and measured displacements

MicroLabBox by a calibration constant. Similar to the numerical studies, the time step and solver adopted in the RTHS were 0.005 seconds, and the ode4 solver, respectively.

### 5.2 Phase-lead compensator

One of the most challenging issues for RTHS in this study is to impose a desired displacement on the MR damper accurately and stably without delay. Therefore, delay compensation plays an important role for the performance of RTHS. The phase-lead compensator (PLC) proposed by Chen and Tsai (2013) was adopted to compensate the dynamics of the servo-hydraulic system in this study. The discrete-time PLC was developed by using the weighted linear extrapolation and the inverse model principle. A delay constant $\alpha$ is the only one positive parameter that needs to be assigned for the PLC. The discrete PLC, $C(z)$, can be expressed as

$$C(z)=\frac{\left[W_1+\left(W_1+W_2+1\right)\alpha\right]z^2+\left[W_2-\left(W_1+W_2+1\right)\alpha\right]z+1}{W_1z^2+W_2z+1} \tag{13}$$

where $W_1$ and $W_2$ are the weightings which need to be selected in the stable regions; and $z$ is a complex number in the z transform. In this study, both $W_1$ and $W_2$ were set 2, which are located in the stable region. In order to realize the delay constant $\alpha$, three additional tests were performed in which band-limited white noise displacement was used as the displacement command for the actuator. Meanwhile, three different control schemes for the MR damper were applied to observe the delay steps between desired and measured displacements including maximum voltage (0.3 V), minimum voltage (0 V), and random voltages (from 0 V to 0.3 V). The phase plot that illustrates the relationships between the desired and measured displacements is shown in Fig. 13. It is obvious that the phase lag of each test is similar and approximately equal to three delay steps (15 ms) between the desired and measured displacements. Accordingly, the delay constant $\alpha$ was taken as 3 for the PLC. The corresponding transfer function of the PLC is then obtained

$$C(z)=\frac{17z^2-13z+1}{2z^2+2z+1} \tag{14}$$

The block diagram of the RTHS is depicted in Fig. 14 where $x$, $x_c$, and $x_m$ are the desired, compensated, and measured displacements, respectively; and $F_{MR}$ is the MR damper force measured from the load cell of the servo-hydraulic actuator.

### 5.3 Experimental results

The compensation performance of the PLC is evaluated by calculating the root-mean-square (RMS) error between the desired and measured displacements, which can be expressed as

$$\mathrm{RMS_T}(\%)=\sqrt{\frac{\sum_{k=1}^{N}\left(x[k]-x_a[k]\right)^2}{\sum_{k=1}^{N}x_a[k]^2}}\times 100\% \tag{15}$$

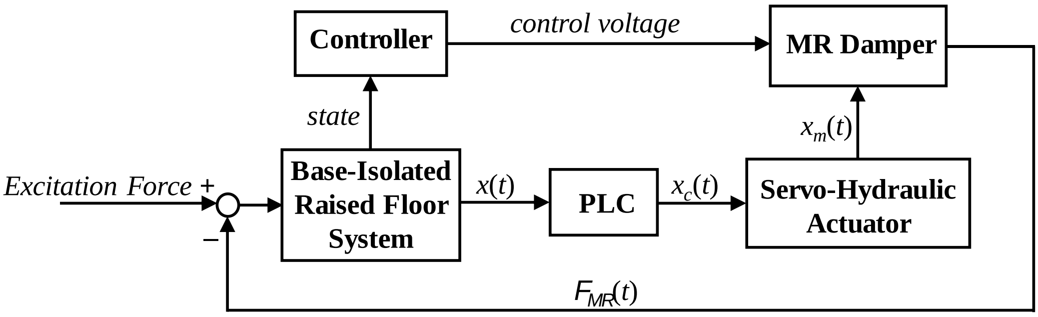


Fig. 14 Block diagram of the RTHS

Table 3 RMS errors of the RTHS

| Input excitation | Control algorithm | Slope angle $\theta$=3$^o$ | Slope angle $\theta$=6$^o$ | Slope angle $\theta$=9$^o$ |
|---|---|---|---|---|
| TAP034_1F | Passive-on | 3.082 | 3.822 | 4.301 |
| | SC | 1.325 | 2.412 | 2.927 |
| | MSC | 1.445 | 2.419 | 2.918 |
| | FLC | 1.574 | 2.452 | 2.480 |
| TAP034_RF | Passive-on | 1.621 | 2.337 | 2.460 |
| | SC | 0.415 | 1.100 | 1.316 |
| | MSC | 1.028 | 1.217 | 1.417 |
| | FLC | 1.009 | 1.347 | 1.534 |
| TCU061_1F | Passive-on | 2.741 | 3.860 | 3.499 |
| | SC | 0.403 | 2.079 | 2.345 |
| | MSC | 0.730 | 2.043 | 2.410 |
| | FLC | 1.589 | 2.131 | 2.464 |
| TCU061_RF | Passive-on | 1.270 | 1.917 | 2.130 |
| | SC | 0.342 | 1.087 | 1.465 |
| | MSC | 0.637 | 1.297 | 1.654 |
| | FLC | 0.883 | 1.427 | 1.552 |
| KAU062_1F | Passive-on | 3.033 | 3.358 | 4.007 |
| | SC | 1.514 | 2.054 | 2.463 |
| | MSC | 1.551 | 2.077 | 2.459 |
| | FLC | 1.563 | 2.038 | 2.384 |
| KAU062_RF | Passive-on | 1.509 | 1.829 | 2.100 |
| | SC | 0.857 | 1.234 | 1.360 |
| | MSC | 0.978 | 1.300 | 1.407 |
| | FLC | 1.094 | 1.339 | 1.503 |

where $x[k]$ and $x_a[k]$ are the desired and the measured displacements at the k$^{th}$ step, respectively. It is realized that better compensation performance leads to smaller RMS errors. The RMS errors of the 72 cases of RTHS are shown in Table 3. Apparently, excellent compensation performance is achieved since the RMS errors are mostly smaller than 3%. Meanwhile, the RMS errors of the passive-on control cases are larger than the other three control cases. It is because larger resistance of the MR damper requires more hydraulic pressure for the actuator. However, the RMS errors of the passive-on control cases remain smaller than 4.5 %, which is considered acceptable for RTHS. The effect of the PLC can be clearly observed in the time-history data as shown in Fig. 15 in which the desired, compensated, and measured displacements are the signals of $x$, $x_c$, and $x_m$ in Fig. 14. It can be found that the PLC compensates the delay of the servo-hydraulic system effectively.

Table 4 Maximum relative displacement and absolute acceleration of the RTHS results ($\theta$=3$^o$)

| Input excitation | Control algorithm | Maximum relative displacement (mm) | Maximum absolute acceleration (m/s$^2$) |
|---|---|---|---|
| TAP034_1F | Passive-on | 75.12 | 1.663 |
| | SC | 132.69 | 1.248 |
| | MSC | 137.11 | 1.193 |
| | FLC | 117.87 | 1.174 |
| TAP034_RF | Passive-on | 200.08 | 1.697 |
| | SC | pounding | pounding |
| | MSC | 260.36 | 1.629 |
| | FLC | 265.47 | 1.588 |
| TCU061_1F | Passive-on | 81.18 | 1.520 |
| | SC | 270.12 | 1.135 |
| | MSC | 180.32 | 1.257 |
| | FLC | 116.40 | 1.129 |
| TCU061_RF | Passive-on | 191.04 | 1.663 |
| | SC | pounding | pounding |
| | MSC | pounding | pounding |
| | FLC | 277.03 | 1.448 |
| KAU062_1F | Passive-on | 72.57 | 1.554 |
| | SC | 109.33 | 1.249 |
| | MSC | 113.11 | 1.248 |
| | FLC | 114.64 | 1.088 |
| KAU062_RF | Passive-on | 185.40 | 1.628 |
| | SC | 274.02 | 1.433 |
| | MSC | 230.56 | 1.434 |
| | FLC | 207.39 | 1.450 |

The maximum relative displacement and absolute acceleration of the protected high-tech equipment with 3-degree, 6-degree, and 9-degree slope angles are listed from Table 4 to Table 6, respectively. Comparing the data in Table 5 with those in Table 2, similar trends can be observed. However, it is obvious that the MR damper contributes larger force in the RTHS than that in the numerical simulation. Modeling a semi-active control device such as a MR damper perfectly is considered extremely difficult. Therefore, the difference between the RTHS and numerical studies demonstrates the necessity of conducting RTHS to evaluate the performance of semi-active control applications. From Table 4 to Table 6, it can be found that the responses at the roof level are constantly lager than those at the first floor level. Pounding occurs merely at the roof level, indicating that the based-isolated raised floor system at high levels needs to be concerned particularly. Meanwhile, larger slope angle leads to larger transmitted acceleration but smaller displacement. This observation is consistent with the mechanism of sloped rolling-type isolation devices. Pounding sometimes occurs at the roof level for the 3-degree slope angle cases even after applying semi-active control force. On the other hand, the transmitted acceleration is larger than 2.0 m/s$^2$ for passive-on control cases when the slope angle is 9 degrees, which may damage the equipment. As a result, a slope angle of 6 degrees is suggested as it strikes a balance between the displacement and the transmitted acceleration of the sloped rolling-type isolation device.

The three semi-active control algorithms reduce the absolute acceleration and enlarge the relative displacement simultaneously. Although relative displacements cannot be suppressed significantly, most of the displacement responses still meet the isolation clearance requirements. Pounding merely occurs at the roof level when switching control algorithm is applied. This is because the SC dissipates the least energy among all the four control algorithms. However, the transmitted acceleration of the SC control case is the smallest as long as pounding does not occur. On the contrary, the displacement of the passive-on control case is the lowest because the control voltage for the MR damper is sustained maximum. However, the transmitted acceleration of the passive-on control case is permanently the largest among all the control algorithms. As a result, there is a tradeoff between the displacement and the transmitted acceleration of the sloped rolling-type isolation device. It is obvious that the MSC and FLC seeks a balance between the displacement and the transmitted acceleration. Experimental results show that the

Table 5 Maximum relative displacement and absolute acceleration of the RTHS results ($\theta$=6°)

| Input excitation | Control algorithm | Maximum relative displacement (mm) | Maximum absolute Acceleration (m/s$^2$) |
|---|---|---|---|
| TAP034_1F | Passive-on | 60.41 | 1.816 |
| | SC | 108.95 | 1.211 |
| | MSC | 110.11 | 1.194 |
| | FLC | 89.11 | 1.323 |
| TAP034_RF | Passive-on | 142.97 | 1.921 |
| | SC | 254.99 | 1.131 |
| | MSC | 227.82 | 1.723 |
| | FLC | 191.12 | 1.704 |
| TCU061_1F | Passive-on | 63.48 | 1.882 |
| | SC | 97.15 | 1.365 |
| | MSC | 96.61 | 1.336 |
| | FLC | 104.11 | 1.390 |
| TCU061_RF | Passive-on | 154.12 | 2.014 |
| | SC | pounding | pounding |
| | MSC | 245.81 | 1.667 |
| | FLC | 201.69 | 1.685 |
| KAU062_1F | Passive-on | 64.58 | 1.831 |
| | SC | 111.90 | 1.279 |
| | MSC | 109.14 | 1.292 |
| | FLC | 106.02 | 1.418 |
| KAU062_RF | Passive-on | 177.64 | 1.913 |
| | SC | 223.26 | 1.467 |
| | MSC | 208.12 | 1.708 |
| | FLC | 213.42 | 1.706 |

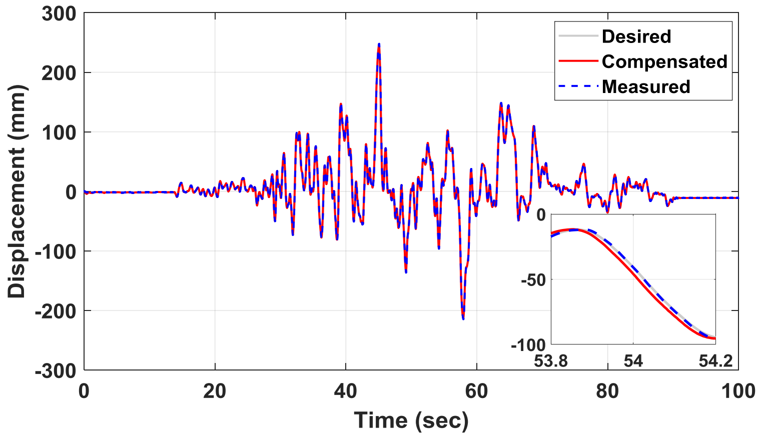


Fig. 15 Effect of the PLC in the time history ((TCU061_RF MSC, $\theta$=6°)

two control algorithms suppress the displacement responses within the isolation clearance (300 mm), which successfully prevent the system from pounding while the transmitted acceleration remains acceptable. Fig. 16 illustrates the relationship between the relative displacements and the absolute accelerations of the base-isolated raised floor system subjected to TCU061_RF excitation with the slope angle of 6 degrees. It can be found that the MSC and FLC only increase the transmitted acceleration when the displacement becomes large. It also demonstrates that the displacement remains

Table 6 Maximum relative displacement and absolute acceleration of the RTHS results ($\theta$=9°)

| Input excitation | Control algorithm | Maximum relative displacement (mm) | Maximum absolute acceleration (m/s$^2$) |
|---|---|---|---|
| TAP034_1F | Passive-on | 51.50 | 2.037 |
| | SC | 90.51 | 1.388 |
| | MSC | 88.16 | 1.379 |
| | FLC | 76.39 | 1.445 |
| TAP034_RF | Passive-on | 127.88 | 2.135 |
| | SC | 240.91 | 1.519 |
| | MSC | 214.42 | 1.940 |
| | FLC | 196.02 | 1.910 |
| TCU061_1F | Passive-on | 70.23 | 2.058 |
| | SC | 95.52 | 1.462 |
| | MSC | 94.44 | 1.465 |
| | FLC | 94.83 | 1.578 |
| TCU061_RF | Passive-on | 156.78 | 2.221 |
| | SC | 232.70 | 1.663 |
| | MSC | 177.28 | 1.938 |
| | FLC | 188.72 | 1.820 |
| KAU062_1F | Passive-on | 50.26 | 2.073 |
| | SC | 103.45 | 1.418 |
| | MSC | 104.67 | 1.401 |
| | FLC | 99.46 | 1.589 |
| KAU062_RF | Passive-on | 166.93 | 2.132 |
| | SC | 234.55 | 1.564 |
| | MSC | 216.42 | 1.936 |
| | FLC | 208.44 | 1.949 |

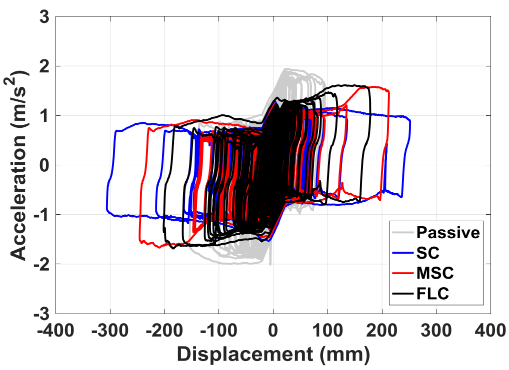


Fig. 16 Displacement-acceleration relationship of the smart base-isolated raised floor system (TCU061_RF, $\theta$=6°)

within the clearance limitation while the absolute acceleration is not increased significantly for the MSC and FLC cases. Conclusively, the smart base-isolated raised floor system can be well-designed by choosing an appropriate slope angle of the base isolation device as well as the control algorithm for the MR damper in order to meet the safety and spatial requirements in real practice.

## 6. Conclusions

In this study, a base-isolated raised floor system with MR dampers was proposed and evaluated in which sloped rolling-type isolation devices were adopted as it has been widely applied to industry for protecting high-tech facilities from damage due to earthquakes in Taiwan. Numerical simulation of the proposed smart base-isolated raised floor system was conducted. A series of identification tests of the MR damper were conducted to build the discrete Bouc-Wen model. Accordingly, four control algorithms can be designed to calculate the control voltage for the MR damper, including passive-on control, switching control (SC), modified switching control (MSC), and fuzzy-logic control (FLC). Compared with the passive-on control performance, the transmitted acceleration of the raised floor system can be reduced after applying the other three controllers. However, the displacement was not suppressed in most cases. In addition, the numerical model could not represent the physical MR damper perfectly as there existed modeling error of the MR damper which cannot be negligible. Therefore, real-time hybrid simulation (RTHS) was adopted to provide an alternative approach to investigate the control performance of the smart base-isolated raised floor system in the study.

For RTHS, the numerical model contained the sloped rolling-type isolation devices, raised-floor system, and high-tech equipment to be protected. The control voltage computed by each control algorithms was sent to the MR damper which was physically tested in the laboratory in real time. Experimental results demonstrate that the MSC and FLC are effective to regulate the relative displacements within the isolation clearance and obtain acceptable increase of the absolute accelerations. Meanwhile, the phase-lead compensator was proved to effectively compensate the time delay. The tracking errors between the desired and achieved displacements were mostly less than 3.0 %. Therefore, the RTHS results were considered accurate and representative. Conclusively, semi-active control of a base-isolated raised floor system offers a feasible solution to mitigate seismic risks of raised floor systems in high-tech industry for real application. A slope angle of 6 degrees with the MSC or FLC is suggested to have balanced control performance between the transmitted acceleration and displacement. Future work will be focused on synthesis of nonlinear controllers to further investigate the feasibility and effectiveness of the raised floor system with sloped rolling-type isolation devices and MR dampers.

## Acknowledgments

This study was supported by the National Center for Research of Earthquake Engineering (NCREE) in Taiwan. The authors would like to thank the funding sponsored by NCREE (06106A2500) the Ministry of Science and Technology, Republic of China (Taiwan) (MOST 105-3111-F-492-002) and all the technical support from NCREE.

## References

AC156 (2010), *Acceptance Criteria for Seismic Qualification by Shake-table Testing of Nonstructural Components and Systems*. ICC Evaluation Service inc.

Bahar, A., Salavati-Khoshghalb, M. and Ejabati, S.M. (2018), "Seismic protection of smart base-isolated structures using negative stiffness device and regulated damping", *Smart Struct. Syst.*, **21**(3), 359-371.

Chae, Y., Kazemibidokhti, K. and Ricles, J.M. (2013), "Adaptive time series compensator for delay compensation of servo-hydraulic actuator systems for real-time hybrid simulation", *Earthq. Eng. Struct. D.*, **42**(11), 1697-1715.

Chai, J.F., Loh, C.H. and Sato, T. (2002), "Modeling of phase spectrum to simulate design ground motions", *J. Chinese Inst. Engineers*, **25**(4), 447-459.

Chen, P.C. and Tsai, K.C. (2013) "Dual compensation strategy for real-time hybrid testing", *Earthq. Eng. Struct. D.*, **42**(1), 1-23.

Cho, S.W., Kim, B.W., Jung, H.J. and Lee, I.W. (2005) "Implementation of modal control for seismically excited structures using magnetorheological dampers", *Journal of Engineering Mechanics (ASCE)*, **131**(2), 177-184.

Darby, A.P., Williams, M.S. and Blakeborough, A. (2002), "Stability delay compensation for real-time substructure testing", *J. Eng. Mech. - ASCE*, **128**(12), 1276 -1284.

Dyke, S.J., Spencer, B.F., Sain, M.K. and Carlson, J.D. (1996) "Modeling and control of magnetorheological dampers for seismic response reduction", *Smart Mater. Struct.*, **5**(5), 565-575.

Friedman, A., Dyke, S.J., Phillips, B.M., Ahn, R., Dong, B., Chae, Y., Castaneda, N., Jiang, Z., Zhang, J., Cha, Y., Ozdagli, A.I., Spencer, B.F., Ricles J.M., Christenson, R., Agrawal, A. and Sause, R. (2015), "Large-scale real-time hybrid simulation for evaluation of advanced damping system performance", *J. Struct. Eng. - ASCE*, **141**(6), 04014150.

Hayati, S. and Song, W. (2017) "An optimal discrete-time feedforward compensator for real-time hybrid simulation", *Smart Struct. Syst.*, **20**(4), 483-498.

Horiuchi, T., Inoue, M., Konno, T. and Namita, Y. (1999), "Real-time hybrid experimental system with actuator delay compensation and its application to a piping system with energy absorber", *Earthq. Eng. Struct. D.*, **28**(10), 1121-1141.

Javanbakht, M. and Amini, F. (2016), "Application of simple adaptive control to an mr damper-based control system for seismically excited nonlinear buildings", *Smart Struct. Syst.*, **18**(6), 1251-1267.

Jung, R.Y., Shing, P.B., Stauffer, E. and Bradford, T. (2007), "Performance of a real-time pseudodynamic test system considering nonlinear structural response", *Earthq. Eng. Struct. D.*, **36**(12), 1785-1809.

Liao, W.I., Chai, J.F., Loh, C.H. and Huang, S.H. (2013), "Seismic performance of raised floor system by shake-table excitations", *Struct. Des. Tall Spec. Build.*, **22**(10), 770-782.

Mamdani, E.H. (1974), "Application of fuzzy algorithms for control of simple dynamic plant", *Proceedings of the Institution of Electrical Engineers*, **121**(12), 1585-1588.

Ramallo, J.C., Johnson, E.A. and Spencer, B.F. (2002), "Smart base isolation systems", *J. Eng. Mech. - ASCE*, **128**(10), 1088-1099.

Shao, X., Lindt, J., Bahmani, P., Pang, W., Ziaei, E., Symans, M., Tian, J. and Dao, T. (2014), "Real-time hybrid simulation of a multi-story wood shear wall with first-story experimental substructure incorporating a rate-dependent seismic energy dissipation device", *Smart Struct. Syst.*, **14**(6), 1031-1054.

Wang, S.J., Hwang, J.S., Chang, K.C., Shiau, C.Y., Lin, W.C., Tsai, M.S., Hong, J.X. and Yang, Y.H. (2014), "Sloped multi-roller isolation devices for seismic protection of equipment and facilities", *Earthq. Eng. Struct. D.*, **43**(10),1443-1461.

Wang, S.J., Yu, C.H., Lin, W.C., Hwang, J.S. and Chang, K.C. (2017), "A generalized analytical model for sloped rolling-type seismic isolators", *Eng. Struct.*, **138**, 434-446.

Zhang, R., Phillips B.M., Taniguchi, S., Ikenaga, M. and Ikago, K. (2017) "Shake table real-time hybrid simulation techniques for the performance evaluation of buildings with inter-story isolation", *Struct. Control Health Monit.*, **24**(10), e1971.

Zheng, L. and Li, Y.N. (2009), “Fuzzy-sliding mode control of a full car semi-active suspension systems with mr dampers”, *Smart Struct. Syst.*, **5**(3), 261-277.

*BS*